



## RESEARCH ARTICLE

# Coupled Lattice Discrete Particle Model for the simulation of water and chloride transport in cracked concrete members

**Yingbo Zhu<sup>1,\*</sup>** | **Dongge Jia<sup>1,\*</sup>** | **John C. Brigham<sup>1,2</sup>** | **Alessandro Fascati<sup>1,2</sup>**

<sup>1</sup>Department of Civil and Environmental Engineering, University of Pittsburgh, Pittsburgh, Pennsylvania, USA

<sup>2</sup>Department of Bioengineering, University of Pittsburgh, Pittsburgh, Pennsylvania, USA

\*Co-first authors

## Authorship

Yingbo Zhu and Dongge Jia should be considered joint first author.

## Correspondence

Alessandro Fascati, Department of Civil and Environmental Engineering, University of Pittsburgh, 3700 O'Hara Street, Pittsburgh, PA 15261, USA.  
Email: [fascati@pitt.edu](mailto:fascati@pitt.edu)

## Funding information

The findings presented herein are based upon work supported by the Impactful Resilient Infrastructure Science & Engineering (IRISE) consortium in the Department of Civil and Environmental Engineering at the University of Pittsburgh.

## ABSTRACT

A novel coupled mechanical and mass transport lattice discrete particle model (LDPM) is proposed to quantitatively assess the impact of cracks on the mass transport properties in concrete members subjected to short- and long-term loading conditions. In the proposed approach, two sets of dual lattice networks are generated: one to resolve the mechanical response and another for mass transport analysis. The cracks predicted by the mechanical lattice are mapped onto the transport elements to investigate the effect of cracks on the global transport properties in the members. The proposed model is capable of describing both convection and diffusion mechanisms, and a new quantitative relationship is proposed for the estimation of the diffusion coefficient based on local crack information. Moreover, creep behavior is incorporated to account for the influence of cracks induced by long-term loading conditions. Numerical results, in the form of dynamic changes in cumulative water and chloride contents in concrete members under tension, compression, and bending with various stress levels show remarkable accuracy when compared to available experimental observations. The proposed model provides an effective means for incorporating mesoscale information in predictions of water and chloride transport in concrete members under varying short- and long-term loading conditions.

## 1 | INTRODUCTION

Chloride-induced corrosion in reinforced concrete members has been recognized as one of the most significant reasons for structural deterioration in civil infrastructure. According to a report by the US Federal Highway Administration (Federal Highway Administration, 2002), the annual cost of corrosion for mitigation and rehabilitation related to concrete highway bridges was approximately \$8.3 billion; furthermore, the study estimated that indirect costs to users, such as traffic delays and lost productivity, were up to 10 times the direct corrosion costs. The presence and evolution of cracking in concrete promote faster ingress of aggressive ions from the surface to the interior, affecting both the performance and durability of the concrete itself and reinforcements (Ismail et al., 2004). This intrusion, in turn,

can further exacerbate cracking and result in substantial deterioration of concrete, particularly in aggressive environments characterized by freeze-thaw cycles (Yang et al., 2006). In this context, the complex interactions between mechanical degradation and penetration of aggressive ions pose considerable scientific challenges in the definition of predictive models and computational approaches for the simulation of the coupled effects. Consequently, quantifying the impact of cracking on the transport properties of concrete has been a central focus in civil engineering research over the last decades.

Considerable experimental research has been conducted to quantitatively characterize the influence of cracking on transport characteristics in concrete composites (Y. Li et al., 2016; Lim et al., 2000; J. Liu et al., 2017; L. Zhang et al., 2014). At the same time, computational methods have also

\*\*\*

\*\*\*

been explored in the past two decades, both as a complement to experimental tests and a tool for further discovery of the underlying physical processes. The majority of numerical studies in this field were performed based on finite element analysis (FEA) and use mesoscale models of heterogeneous concrete consisting of aggregates, matrix, and/or Interfacial Transition Zone (ITZ). For example, available works (Bentz et al., 2013; Y. Li et al., 2016; Peng et al., 2019; Qiu & Dai, 2021) presented 2D multi-phase concrete models with user-defined cracks to study the influence of crack width and height on chloride transport (CT) properties. Literature (Abeyaneh et al., 2016) reported a 3D two-phase concrete model with randomly placed microcracks at the interface between aggregate and matrix to explore the effect of microcrack widths on CT properties. To address the limitations of using user-defined cracks in the simulations, coupled FEA models have been proposed more recently. In 2020, Literature (W. Li & Guo, 2020) applied peridynamics to the simulation of the crack evolution of 2D multi-phase concrete members under various types of external loading, with the goal of investigating the effects of crack networks on chloride penetration. The proposed approach was proven to be capable of assessing the influence of different types of loading on CT in concrete. Similar work was undertaken by Liu et al. (Q. Liu et al., 2022), where crack propagation in a 2D model under tension was captured by the extended finite element method. To achieve a more realistic representation of cracks, a 3D concrete model, reflecting the morphology of real aggregates, was built by using the spherical harmonic theory (Zheng et al., 2022), and then the cracks captured by a damage constitutive law were used to analyze the CT properties. More recently, Literature (Tong et al., 2024) created a 3D microstructure to investigate the chloride transport in concrete.

Another viable alternative for simulating the mass transport process in concrete materials is the adoption of discrete methods based on a lattice modeling approach (Grassl, 2009; Šavija et al., 2013). The lattice elements, representing the mortar paste connecting two nearby particles (i.e., the coarse aggregates), can serve as conduits for mass transport, providing a mesoscale framework for flow analysis in cementitious composites. In the early stages, lattice models were employed to simulate flow permeability and water absorption in cracked concrete members (Grassl, 2009). Further advancements extended capabilities of the approach to predict the CT process in cracked concrete members (Šavija et al., 2013, 2014). Although the proposed model exhibited good agreement with experimental results, it did not consider the nonlinear behavior of the material. In this model, elastic properties were assigned to all phases of concrete material, and cracks were simulated by removing the lattice elements once their ratio of stress/strength exceeded a predefined threshold. While most research only considered the chloride diffusion mechanism, Wang et al. (L. Wang et al., 2016) investigated both the chloride diffusion

and convection mechanism on the CT based on a 2D lattice network model with prescribed cracks. More recently, literature(Tran et al., 2021) proposed a 2D mesoscale mechanical-transport lattice network model to simulate the water and chloride diffusion properties of concrete subjected to compressive loading. The flexibility of this model is limited by the introduced compressive damage variable to characterize the degree of damage in the material. This is primarily because, at the mesoscopic scale, damage in concrete is caused by the tensile and shear stress interactions, while material under volumetric compression exhibits hardening behavior.

While dual lattice approaches have been proposed in the past to simulate the combined effects of crack networks on the transport properties in different geomaterials (Cibelli et al., 2023; Fascetti & Oskay, 2019b; Grassl & Bolander, 2016; W. Li et al., 2018), no currently available work provided approaches capable of describing this Multiphysics phenomena at the mesoscopic level in plain concrete members, which is one of the main strengths of the LDPM approach. Moreover, the presented literature indicates numerical investigations into the effect of loading-induced cracks on the CT in concrete are limited, whether through FEA or lattice network models, as a result of the significant challenges associated with the description of the complex multiphysics aspects of the phenomenon (Bousikhane et al., 2018; Eliáš & Cusatis, 2022). The first challenge lies in the integration of mechanical and transport models. Although some mechanical models have been coupled with transport models to explore the impact of loading-induced cracks, these models are typically tailored to specific loading scenarios. Concrete structures, however, can suffer damage from various types of loads, and the developed models need to provide flexibility and generalizability to provide robust predictions. Second, modeling CT in unsaturated concrete poses several complexities. The transport process involves convection dominating the early stages, followed by diffusion-dominated effects once the concrete is saturated. The water content is a key parameter that influences the velocity of chloride intrusion, while the majority of available models neglect the convective effects induced by capillary absorption. The third challenge is related to the quantification of the effects of damage/cracks caused by long-term loading on the CT. Long-term loadings contribute to damage evolution in concrete members, potentially leading to substantial crack propagation. Such processes can create preferential pathways and channels for fluid and ion ingress and, in turn, cause further damage. Another significant challenge is how to quantify the influence of microcracks distributed throughout the entire specimen on global diffusion properties. Concrete is a highly heterogeneous material that can develop not only visible main cracks but also numerous microcracks (which cannot be observed by the naked eye) that significantly affect CT properties. Previous research predominantly concentrates on the impact of main cracks or user-defined cracks on the local diffusion

characteristics within the vicinity of these cracks while overlooking the influence of microcracks.

- To overcome the aforementioned challenges, a coupled LDPM approach is presented in this study to accurately assess the effect of cracking on the transport properties in concrete members subjected to various types of short- and long-term loadings. Fundamental novelty presented in this study and major contributions can be summarized as follows:
- (1) A dual 3D LDPM is developed for coupled mechanical and water chloride transport simulations. The mechanical lattice is used to predict the nonlinear behavior of concrete members, after which a novel formulation for transport lattice network model is presented and exercised to analyze the mass transport properties in cracked concrete by mapping crack information calculated by the former model onto the transport elements.
  - (2) The proposed approach incorporates long-term behavior in coupled transport simulations, providing comprehensive insights into the effect of both short- and long-term loading-induced cracking on the CT properties.
  - (3) A novel formulation for evaluating chloride diffusivity in the presence of microcracks is proposed, which can assess concrete components with various stress levels.
  - (4) Water capillary absorption is incorporated in the coupled model, facilitating consideration of both convection and diffusion of CT in unsaturated concrete.

## 2 | COUPLED MECHANICAL AND MASS TRANSPORT LDPM

### 2.1 | Dual lattice network topology

In the proposed coupled LDPM, the canonical two-phase

mesoscale structure of concrete is considered, consisting of coarse aggregates and mortar paste. As is customary, the lattice system for the mechanical modeling is constructed through the given particle size distribution in the material, Delauney tetrahedralization, and modified Voronoi tessellation, as depicted in Figures 1(a-d). The details regarding the generation of mechanical lattice networks can be found in the literature (Cusatis et al., 2011; Fascetti et al., 2018; Zhu & Fascetti, 2024).

The mass transport modeling is realized by a set of lattice elements dual to the ones in the mechanical lattice system. In contrast to the mechanical lattice elements, which connect a pair of adjacent aggregates, transport elements are defined around the volume of aggregates, under assumption of aggregate conductivity being significantly lower than that of the mortar. The transport network is generated by LDPM tessellation (Cusatis et al., 2011), as follows (see Figure 1(f)): the effective volume centroid  $T$  is defined as the point at which all contact facets in a tetrahedron intersect, while the points  $F_i$  ( $i = 1,2,3,4$ ) are defined as the centroids of each surface of the tetrahedron. The transport lattice elements in each tetrahedron are obtained by connecting points  $T$  and  $F_i$  for each tetrahedron face (i.e.,  $\overline{TF}_1, \overline{TF}_2, \overline{TF}_3, \overline{TF}_4$ ), as shown in Figure 1(f), resulting in 4 transport lattice elements per tetrahedron. By employing such tessellation, the transport lattice elements are constructed to be orthogonal to the direction of potential crack paths, as predicted by the corresponding mechanical lattice elements. Therefore, the influence of local cracks on mass transport can be directly described in a discrete fashion, this being one of the significant features of the coupled LDPM approach proposed herein.

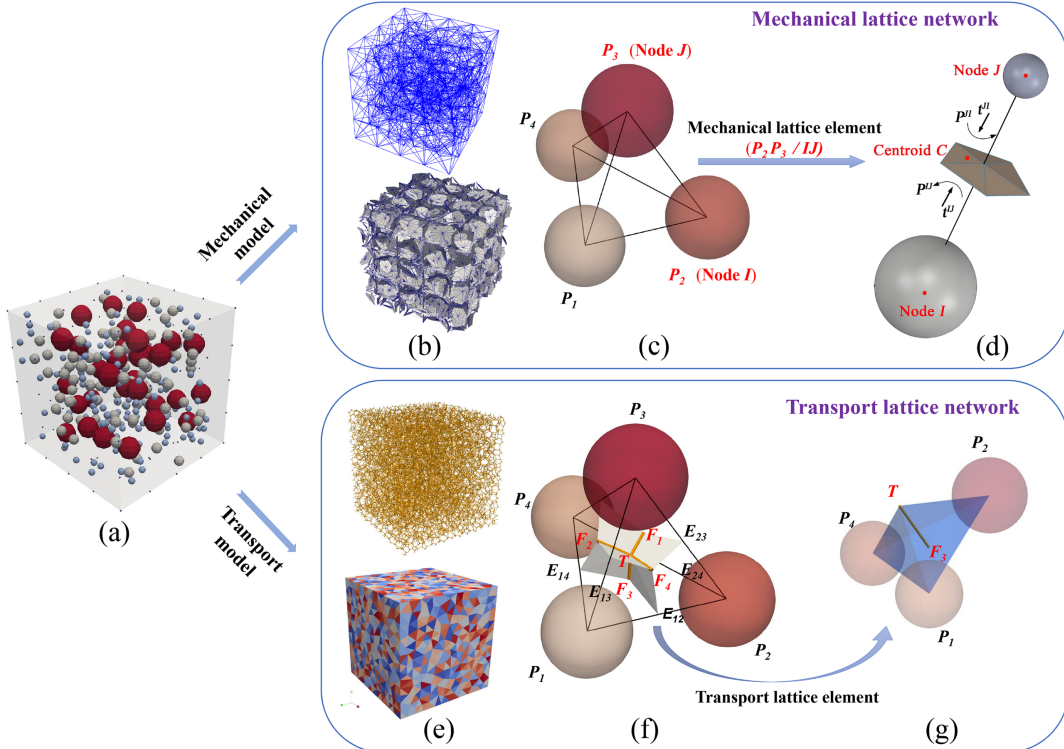
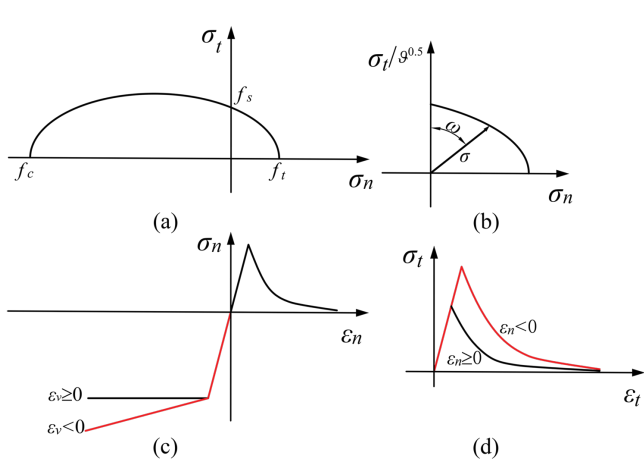


**FIGURE 1**  
Dual lattice network topology: (a) random placement of particles; (b) mechanical lattice struts and facets; (c) tetrahedron consisting of particles and lattice struts; (d) degrees of freedom and the facet of a lattice element; (e) transport lattice network and transport cells; (f) transport lattice element dual to the Delaunay; (g) transport lattice element and the volume it represents.



$$\begin{aligned} &\text{Elliptical bounding surface} \\ &\sigma_n(\sigma_n - f_c - f_t) - \frac{f_c f_t}{f_s^2} \sigma_t^2 + f_c f_t = 0 \quad (\text{F1}) \\ &\text{Tensile softening behavior} \\ &\sigma_b(\omega) = \sigma_0 e^{-\frac{-H}{\sigma_0}(<\epsilon_1 - \epsilon_0>)} \quad (\text{F2}) \\ &H(\omega) = H_s + (H_t - H_s) \left( \frac{2\omega}{\pi} \right)^{n_t} \quad (\text{F3}) \\ &H_s = H(\omega = 0) = \frac{2E_t}{(2E_t G_s)/(f_s^2 l^e) - 1} \quad (\text{F4}) \\ &H_t = H\left(\omega = \frac{\pi}{2}\right) = \frac{2E_n}{(2E_n G_t)/(f_t^2 l^e) - 1} \quad (\text{F5}) \\ &\text{Compressive hardening behavior} \\ &\sigma = \begin{cases} f_c & \epsilon_v \geq 0 \\ f_c e^{\frac{H}{f_c}(-\epsilon_v - \epsilon_c)} & \epsilon_v < 0 \end{cases} \quad (\text{F6}) \\ &H = \frac{H_c}{1 + \frac{\epsilon_v}{\epsilon_D}} \quad (\text{F7}) \\ &\text{Frictional behavior} \\ &\sigma = \sigma_{t,0} e^{\frac{-H}{\sigma_{t,0}} <\epsilon_t - \epsilon_{t,0}>} \quad (\text{F8}) \\ &H(\omega) = H_s - H_s \left( \frac{-2\omega}{\pi} \right)^{n_c} \quad (\text{F9}) \end{aligned}$$

**FIGURE 2**  
Constitutive laws adopted for the mechanical lattice: (a) elliptical bounding surface of  $\sigma_n - \sigma_t$  curves; (b) parameter  $w$  in terms of  $\sigma_n$  and  $\sigma_t$ ; (c) compressive and tensile behavior; (d) shear behavior.

## 2.2 | Mechanical LDPM with creep behavior

### 2.2.1 | Strain compatibility

In LDPM simulations, each particle is assumed to undergo rigid body motion. The displacement jump ( $[\mathbf{u}]$ ) at the centroid of each resisting area (point  $C$  in Figure 1(d)) can therefore be expressed by:

$$[\mathbf{u}] = \mathbf{u}^J - \mathbf{u}^I + \boldsymbol{\theta}^J \times \mathbf{C}^J - \boldsymbol{\theta}^I \times \mathbf{C}^I \quad (1)$$

Based on such measure, the strain ( $\epsilon_\alpha$ ) and curvature ( $\kappa$ ) in each lattice element is obtained as:

$$\begin{cases} \epsilon_\alpha = \frac{[\mathbf{u}]}{l_e} \cdot \mathbf{e}_\alpha \\ \kappa = \frac{(\boldsymbol{\theta}^J - \boldsymbol{\theta}^I)}{l} \cdot \mathbf{e}_\alpha \end{cases} \quad (2)$$

where  $\mathbf{u}^I, \boldsymbol{\theta}^I$  and  $\mathbf{u}^J, \boldsymbol{\theta}^J$  are the translation and rotation vectors at Node  $I$  and Node  $J$ , respectively;  $\mathbf{C}^I$  and  $\mathbf{C}^J$  are the vectors connecting Nodes  $I$  and  $J$  to the Centroid  $C$ ;  $\mathbf{e}_\alpha$  is the unit vector that defines the local coordinates of each lattice strut,  $\alpha = n, l, m$ ;  $l_e$  is the length of the lattice element.

In structural applications, CT in concrete components is a process that evolves at larger temporal scales than mechanical damage (Abdellatef et al., 2019; Di Luzio & Cusatis, 2013).

Therefore, in order to capture degradation mechanisms in a coupled framework, it is essential to consider the creep response of concrete in the analyses. It should be mentioned that in this study the mechanical LDPM only takes into account purely viscous strain while neglecting viscoelastic strain. This simplification is based on the assumption that the effect of external loading on mass transport properties is fundamentally governed by the presence of cracks, while the viscoelastic strain is considered to have limited influence on the development of cracks (Sciumè & Benboudjema, 2017). The total facet strain rate of each lattice element is estimated by the addition of the short-term strain rate  $\dot{\varepsilon}_{\alpha,ed}$  and the time-dependent purely viscous strain rate  $\dot{\varepsilon}_{\alpha,v}$ :

$$\dot{\varepsilon}_\alpha = \dot{\varepsilon}_{\alpha,ed} + \dot{\varepsilon}_{\alpha,v} \quad (3)$$

The viscous strain rate is defined according to (Abdellatif et al., 2019):

$$\dot{\varepsilon}_{\alpha,v} = \xi \kappa \phi S G \sigma_\alpha \quad (4)$$

where  $\xi$  and  $\kappa$  are model parameters,  $\xi$  is usually determined by calibrating models with experimental results (unit: MPa $^{-1}$ ), and  $\kappa$  is assumed as  $2 \times 10^{-8}$  (MPa · day) $^{-1}$ ;  $\phi = (0.1 + 0.9h^2)\exp(Q_s/R(1/T_0 - 1/T))$  is an environmental parameter associated with temperature  $T$ ,  $h$  is the relative humidity and  $Q_s/R \approx 5000$  °K. For all analyses herein, the temperature  $T$  is equal to the reference room temperature  $T_0$ , while the relative humidity  $h$  for concrete specimens is equal to 1 during all the immersion test;  $S$  is the microprestress calculated by solving the differential equation  $\dot{S} + \phi \kappa S^2 = \kappa_1 [\dot{T} \ln(h) + T \dot{h}/h]$ ;  $\kappa_1$  is a model parameter related to the drying viscous behavior;  $\sigma_\alpha$  is the stress acting on the lattice strut, which only accounts for the short-term strain of  $\dot{\varepsilon}_{\alpha,ed}$ ;  $G = 1$  if  $\alpha = n$  and  $G = 1/\vartheta$  if  $\alpha = l, m$ .

### 2.2.2 | Constitutive law

At the elastic stage, the normal and tangential stresses are  $\sigma_n = E_n \varepsilon_n^{IJ}$ ,  $\sigma_t = E_t \varepsilon_t^{IJ} = \vartheta E_n \varepsilon_t^{IJ}$ , where  $\varepsilon_n^{IJ}$  and  $\varepsilon_t^{IJ} = \sqrt{\varepsilon_l^{IJ2} + \varepsilon_m^{IJ2}}$  are the normal and tangential strain measures of each lattice element, respectively;  $E_n$  and  $E_t = \vartheta E_n$  are the lattice-level normal and shear moduli, respectively;  $\vartheta = (1 - 4\nu)/(1 + \nu)$  is a shear-normal coupling parameter for lattice elements at the mesoscopic scale, which is related to the macroscopic Poisson's ratio  $\nu$ .

To simulate inelastic behavior, an elliptical stress boundary surface is defined (Fascetti et al., 2018):

$$\sigma(\omega) = \frac{\sin \omega (f_c + f_t) + \sqrt{D}}{2 \left( \sin \omega^2 - \frac{\cos \omega^2 \vartheta f_c f_t}{f_s^2} \right)} \quad (5)$$

where  $\sigma = \sqrt{\sigma_n^2 + \sigma_t^2}/\vartheta$  and  $\varepsilon = \sqrt{\varepsilon_n^2 + \vartheta \varepsilon_t^2}$  are defined as the effective stress and strain measures, respectively;  $\omega = \arctan(\varepsilon_n/\sqrt{\vartheta} \varepsilon_t)$  is the coupling strain;  $D = [\sin \omega (f_c + f_t)]^2 - 4f_c f_t (\sin \omega^2 -$

$$\cos \omega^2 \vartheta f_c f_t/f_s^2)$$
.

Nonlinear constitutive laws for each lattice element are defined in terms of three different stress-strain conditions: (1) cohesive behavior due to tension and shear; (2) hardening behavior under multi-axial compression; and (3) frictional behavior resulting from interacting compressive and shear actions. A brief illustration of the constitutive laws without showing the unloading-reloading paths is given in Figures 2(c)-(d). As presented in (Fascetti et al., 2018), the choice of an elliptical stress boundary surface allows for the definition of formal rules to enforce energy dissipation at the lattice element level exactly, as well as a continuous transition in the softening/hardening parameter  $H$  (see Figure 2). For the full details on the constitutive model, the reader is referred to (Fascetti et al., 2018, 2022; Jia et al., 2024).

## 2.3 | Mass transport model

The CT mechanism in the early transport stage (i.e., before saturation of concrete components) is predominantly convective, as a result of capillary absorption. This stage is followed by diffusion-dominated behavior, once the concrete approaches full saturation. In addition, the chloride diffusion properties are significantly influenced by the water content in unsaturated concrete (de Vera et al., 2007; Y. Zhang et al., 2018). To this end, all the aforementioned aspects (i.e., water transport, convection, chloride diffusion) need to be described by the numerical models. The specific implementation proposed herein is presented in the next sections.

### 2.3.1 | Water transport

The 1D Richards' equation derived from Darcy's law and the mass conservation law for unsaturated flow within porous material is expressed as (Lockington et al., 1999):

$$\frac{\partial \theta}{\partial t} = \frac{\partial}{\partial x} \left( D_w(\theta) \frac{\partial \theta}{\partial x} \right) \quad (6)$$

where  $\theta$  is the relative water content, defined as  $\theta = (\theta - \theta_i)/(\theta_s - \theta_i)$ ;  $\theta$ ,  $\theta_i$  and  $\theta_s$  are the water contents at the current stage, its reference value at the start of the simulations, and at complete saturation, respectively;  $D_w$  is the water diffusivity coefficient, which is a material property influenced both by the material mixture and the relative water content. Previous works (Hall, 1989; Lockington et al., 1999) proposed an exponential law to estimate diffusivity in unsaturated concrete in the absence of mechanical damage:

$$D_w(\theta) = D_{w,0} e^{n\theta} \quad (7)$$

where  $n$  is an empirically estimated constant representing the shape of diffusivity curves (typically,  $n = 6 \sim 9$ ), while  $D_{w,0}$  is the value of the diffusion coefficient in dry conditions. Since direct measurement of  $D_{w,0}$  is challenging, its value is usually estimated from the material's sorptivity  $S$  (Lockington, 1993; Lockington et al., 1999), as shown in Equation (8).

Additionally, experimental findings (L. Wang & Li, 2014; Yang et al., 2006) have shown that the initial water absorption (first 2~4 hours) is larger than that observed at later stages. Therefore, this study proposed the use of a scaling parameter  $\rho$  ( $\rho = 2.5$  for all analyses shown herein) describing this mechanism:

$$D_{w,0} = \begin{cases} \frac{1}{123.13} \left( \frac{S}{\theta_s - \theta_i} \right)^2, & t < 120\text{min} \\ \frac{1}{123.13\rho} \left( \frac{S}{\theta_s - \theta_i} \right)^2, & t \geq 120\text{min} \end{cases} \quad (8)$$

The effect of a crack on diffusivity is accounted for by incorporating the quadratic element law for water flow in a crack (Y. Zhang et al., 2019), which is given as:

$$D_w(\theta, w_c) = \left( D_{w,0} + \frac{w_c^2 p_r}{12\eta} \right) e^{n\theta} \quad (9)$$

where  $w_c$  is the crack width;  $\eta$  is the viscous dynamic coefficient of water (0.001 Pa·s);  $p_r$  is the reference pressure, determined as 18.62 N/mm<sup>2</sup> by fitting with the experimental capillary curves for ordinary Portland cement (OPC) (L. Wang et al., 2016). Moreover, the value of  $D_w(\theta, w)$  is capped at the value of 1 in the numerical models, to avoid unrealistically large values resulting from extremely large cracks.

### 2.3.2 | Chloride transport

CT in unsaturated concrete, considering both the convection and diffusion effects, can be described by:

$$\frac{\partial C_t}{\partial t} = \nabla \cdot (D_{cl}(\theta) \nabla C_f) + C_f \frac{\partial \theta}{\partial t} \quad (10)$$

where  $D_{cl}$  is the chloride diffusivity coefficient;  $C_t = C_f + C_b$  is the total chloride concentration, consisting of the free concentration  $C_f$  and bound chloride concentration  $C_b$ . By introducing the chloride binding capacity  $\lambda = \partial C_b / \partial C_f$ , the change of chloride concentration with time can be expressed as:

$$\frac{\partial C_t}{\partial t} = \frac{\partial C_f}{\partial t} + \frac{\partial C_b}{\partial t} = (1 + \lambda) \frac{\partial C_f}{\partial t} \quad (11)$$

The chloride binding capacity  $\lambda$  is a material property, which can be expressed as (Xi & Bažant, 1999):

$$\lambda = 10^B \frac{A_0 \beta_{gel}}{35450 \beta_{sol}} \left( \frac{C_f}{35.45 \beta_{sol}} \right)^{A_0-1} \quad (12)$$

where  $A_0$  and  $B$  are material constants, 0.38 and 1.14 for OPC, respectively;  $\beta_{sol}$  is the ratio of pore solution to concrete, measured in liters of pore solution per gram of concrete (L/g), and  $\beta_{gel}$  is the ratio of C-S-H gel to concrete, in terms of grams of C-S-H gel per gram of concrete (g/g).

The values of  $\beta_{sol}$  and  $\beta_{gel}$  can be determined from the water-to-cement ratio and the specific mix proportion.

At the 1-dimensional level of the transport lattice elements, the CT process is described by the following governing equation, obtained from combining Equations (10) and (11):

$$\frac{\partial C_f}{\partial t} = \underbrace{\frac{C_f}{1 + \lambda(C_f)} \frac{\partial}{\partial x} \left( D_w(\theta) \frac{\partial \theta}{\partial x} \right)}_{\text{Convection}} + \underbrace{\frac{1}{1 + \lambda(C_f)} \frac{\partial}{\partial x} \left( D_{cl}(\theta) \frac{\partial C_f}{\partial x} \right)}_{\text{Diffusion}} \quad (13)$$

The exponential law for determining the chloride diffusivity  $D_{cl}$  in unsaturated concrete material, as proposed in the literature (Saeki & Niki, 1996; L. Wang & Ueda, 2014), is employed herein:

$$D_{cl}(\theta) = D_{cl,0} 0.0032 \times 10^{2.5\theta} \quad (14)$$

where  $D_{cl,0}$  is the chloride diffusivity in the saturated concrete in the absence of cracking.

Two empirical relationships (Djerbi Tegguer et al., 2013; Šavija et al., 2013) have been proposed in the past to quantify the influence of the crack width ( $w_c$ ) on the chloride diffusivity caused by cracking ( $D_{cl,c}$ ) based on experimental or numerical calibration results. The primary limitation of these relationships is that they estimate changes in local diffusivity in concrete with large crack widths while ignoring the influence of small cracks and microcracks. However, cementitious materials have been proven to form considerable microscopic crack networks, which are generally undetectable by naked eye, even under low-magnitude loading conditions [4]. These microcracks can significantly increase the global diffusion properties of materials by creating more transport conduits and changing the local porosity. This assumption has been verified in the literature, with several experimental observations (Lim et al., 2000; J. Liu et al., 2017; L. Zhang et al., 2014) reporting that the CT velocity in concrete members under low tensile/compressive stresses for which no obvious cracks were observed, exhibited significant increases when compared with that of the unstressed specimens. To address this challenge, this study proposes a new relationship for accounting for the change diffusivity induced by both micro- and macro-cracks in the domain:

$$D_{cl,c}(\theta, w_c) = \begin{cases} D_{cl}(\theta) e^{aw_c}, & w_c < 10\mu\text{m} \\ D_{fc}, & w_c \geq 10\mu\text{m} \end{cases} \quad (15)$$

where  $D_{cl,c}$  is chloride diffusivity for damaged material; the parameter  $a = \exp(D_{fc}/D_{cl}(\theta))/10$  for the sake of achieving a smooth transition between the two-phase relationship;  $D_{fc}$  is the constant diffusivity value associated with macroscopic cracks (i.e.,  $w_c \geq 10\mu\text{m}$ ), and it is calibrated as  $D_{fc} = 2.8 \times 10^{-10} \text{ m}^2/\text{s}$  in this study, and will be validated later.

## 3 | NUMERICAL IMPLEMENTATION

### 3.1 | Discretization of mass transport model

The governing equations for water and chloride transport analysis are similar in form, both requiring discretization in spatial and temporal domains. To avoid redundancy, only the discretization process for the water transport equation is described herein. Employing the Galerkin weighted residual method and substituting the spatial discretization into the governing equation of Equation (6) yields a discrete form for water transport analysis for each element (Fascetti & Oskay, 2019a; Z. Wang et al., 2024):

$$\mathbf{M}_e \frac{d\boldsymbol{\theta}}{dt} + \mathbf{K}_e(\boldsymbol{\theta}_e)\boldsymbol{\theta}_e - \mathbf{f}_e = \mathbf{0} \quad (16)$$

where  $\mathbf{K}_e$  and  $\mathbf{M}_e$  are the diffusivity and mass matrices, respectively;  $\mathbf{f}_e$  is the forcing vector;  $\boldsymbol{\theta}_e$  is the relative water content of a transport lattice element, which is calculated by averaging the relative water content at its two nodes. The form of the elemental matrices is given by (Fascetti & Oskay, 2019a; Grassl & Bolander, 2016):

$$\begin{aligned} \mathbf{K}_e = \int_{\Omega^e} \mathbf{B}^T D_w(\boldsymbol{\theta}_e) \mathbf{B} d\Omega^e &= \xi_1 \int_{l_e} D_w(\boldsymbol{\theta}_e)(x) A_e(x) \mathbf{B}^T \mathbf{B} dx \\ &= \frac{\xi_1 D_w(\boldsymbol{\theta}_e) A_e^*}{3l_e} \begin{bmatrix} 1 & -1 \\ -1 & 1 \end{bmatrix} \end{aligned} \quad (17)$$

$$\begin{aligned} \mathbf{M}_e = \int_{\Omega^e} \mathbf{N}(\mathbf{x})^T \mathbf{N}(\mathbf{x}) d\Omega^e \\ = \xi_2 \int_{l_e} (x) A_e(x) \mathbf{N}(x)^T \mathbf{N}(x) dx = \frac{\xi_2 A_e^* l_e}{30} \begin{bmatrix} 1 & 1.5 \\ 1.5 & 6 \end{bmatrix} \end{aligned} \quad (18)$$

$$\mathbf{f}_e = - \int_{\Gamma_q^e} \mathbf{q} \mathbf{N}^T(\mathbf{x}) d\Gamma_q^e = \begin{bmatrix} 0 \\ -q_L A_e^* \end{bmatrix} \quad (19)$$

The evaluation of the cross-sectional area requires special treatment in view of the fact that the transport elements are non-prismatic. To this end,  $A_e^*$  is defined as the cross-sectional area at the endpoint of a transport lattice element (i.e., the area formed by points  $P_1 P_2 P_4$  for the transport element  $\overline{TA}$ , see Figure 3); the volume centroid  $T$  is defined as the starting point of a transport element, while the ending point is the surface point (e.g., points A and B in Figure 3);  $A_e(x) = A_e^*(x - x_A)^2 / l_e^2$  is the cross-sectional area at an arbitrary point along the length of the transport lattice element, and  $x$  is the curvilinear abscissa associated with the element.

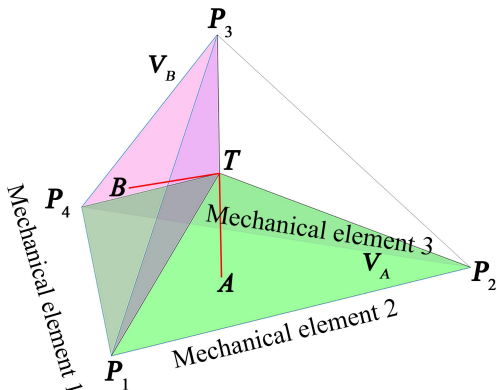


**FIGURE 3** Diagram of the crack mapping between mechanical and transport lattice elements.

Following the assumption that the diffusivity of the coarse aggregate particles is negligible when compared to that of the mortar, the cross-sectional area of each transport element should not include the volume occupied by particles. To this end, volume reduction factors  $\xi_1$  and  $\xi_2$  are introduced in the element diffusion and mass matrices to account for the presence of aggregates. Since the components of the diffusion matrix are of the same order as the element length, the volume reduction factor  $\xi_1$  for  $\mathbf{K}_e$  is defined as  $\xi_1 = (1 - v_{ae})^{1/3}$ , where  $v_{ae}$  is the volume fraction of aggregate in the mix. Alternatively, the components of the mass matrix are of the same order as the elemental volume, therefore, the  $\xi_2$  for  $\mathbf{M}_e$  is defined as  $\xi_2 = 1 - v_{ae}$ .

Discretization in time is performed by means of the Crank-Nicolson method, which is an unconditionally stable method subject to a maximum time stepping criterion (Fascetti & Oskay, 2019a):

$$(17) \left[ \frac{\mathbf{K}_e^{t+\Delta t}}{2} + \frac{\mathbf{M}_e}{\Delta t} \right] \boldsymbol{\theta}(t + \Delta t) = \left[ -\frac{\mathbf{K}_e^t}{2} + \frac{\mathbf{M}_e}{\Delta t} \right] \boldsymbol{\theta}(t) - \frac{(\mathbf{f}_e^{t+\Delta t} + \mathbf{f}_e^t) \Delta t}{2} \quad (20)$$

$$\Delta t_{max} = \frac{l_{e,min}^2}{2D_w} \quad (21)$$

where  $\Delta t_{max}$  is the maximum time step and  $l_{e,min}$  is the minimum length of transport lattice elements in the domain.

### 3.2 | Coupling and algorithmic procedure

Figure 4 graphically depicts the algorithm utilized in the proposed coupled LDPM. A central difference scheme is utilized to integrate the equation of motion, while Crank-Nicolson method is used for the mass transport analysis, as described above. This results in different time stepping requirements for the two analyses. Moreover, when modeling the mechanical response of concrete under short-term loading, a displacement-control scheme is used to capture the strain-softening behavior, whereas, for long-term loading conditions, force-control is employed. Based on Equation (4), the purely viscous strain at time  $t$  ( $\varepsilon_{\alpha,v}^t$ ) can be calculated by:

$$\varepsilon_{\alpha,v}^t = \varepsilon_{\alpha,v}^{t-\Delta t} + \Delta t \xi \kappa \phi S^t G \sigma_{\alpha}^{t-\Delta t} \quad (22)$$

$$S^t = S^{t-\Delta t} - \phi_s \kappa (S^{t-\Delta t})^2 \Delta t + \kappa_1 \left[ \Delta T \ln(h) + \frac{T \Delta h}{h} \right] \quad (23)$$

where  $\varepsilon_{\alpha,v}^{t-\Delta t}$  is the viscous strain at the previous step;  $S^t$  and  $S^{t-\Delta t}$  are the microprestresses in the mechanical lattice elements at the current and previous step, respectively.

The crack width in each mechanical lattice element ( $w_{mech}$ ) is calculated as follows (Fascetti et al., 2018):

$$w_{mech} = \sqrt{w_n^2 + w_t^2} \quad (24)$$

where  $w_n = l_e(\varepsilon_n - \sigma_n/E_n)$  and  $w_t = l_e(\varepsilon_t - \sigma_t/E_t)$  are the normal and tangential crack openings, respectively; for short-term loading conditions  $\varepsilon_n = \varepsilon_{n,ed}$  and  $\varepsilon_t = \varepsilon_{t,ed}$ , while for long-term loading conditions  $\varepsilon_n = \varepsilon_{n,ed} + \varepsilon_{n,v}$  and  $\varepsilon_t = \varepsilon_{t,ed} + \varepsilon_{t,v}$ .

As shown in Figure 3, each transport element is associated with three mechanical lattice elements in space. Therefore, the crack width of each transport element can be estimated by mapping the crack widths of the three mechanical lattice elements onto the transport element. This choice results in a one-way coupling between the mechanical damage predicted on the mechanical lattice and the transport properties of the dual lattice. To perform such coupling, a procedure conceptually similar to the mapping of local damage in dual lattices, as proposed in (Z. Wang et al., 2024), is adopted. Taking the transport element  $\overline{TA}$  as an example, the mapped crack width ( $w_{trans,TA}$ ) can be calculated by:

$$w_{trans,TA} = \sum_{i=1,2,3} w_{mech,ia} \quad (25)$$

$$w_{mech,i} = \sum_{j=A,B} w_{mech,ij} \quad (26)$$

$$w_{mech,ij} = w_{mech,i} * \frac{V_j}{V_A + V_B} \quad (27)$$

where  $w_{mech,ij}$  ( $i = 1,2,3$ ,  $j = A, B$ ) is the crack width value mapping from the mechanical element  $i$  to the corresponding transport elements  $\overline{Tj}$ ;  $w_{mech,i}$  is the crack width in the mechanical element  $i$ ;  $V_A$  and  $V_B$  are the volumes of the sub-tetrahedra  $TP_1P_2P_4$  and  $TP_1P_3P_4$  for the transport elements  $\overline{TA}$  and  $\overline{TB}$ , respectively.

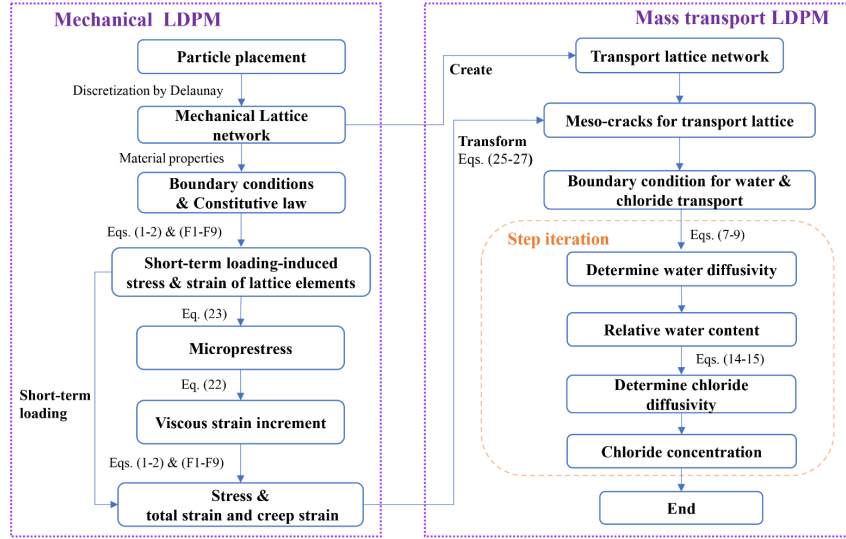


**FIGURE 4**  
Algorithmic procedure of the proposed coupled LDPM model.

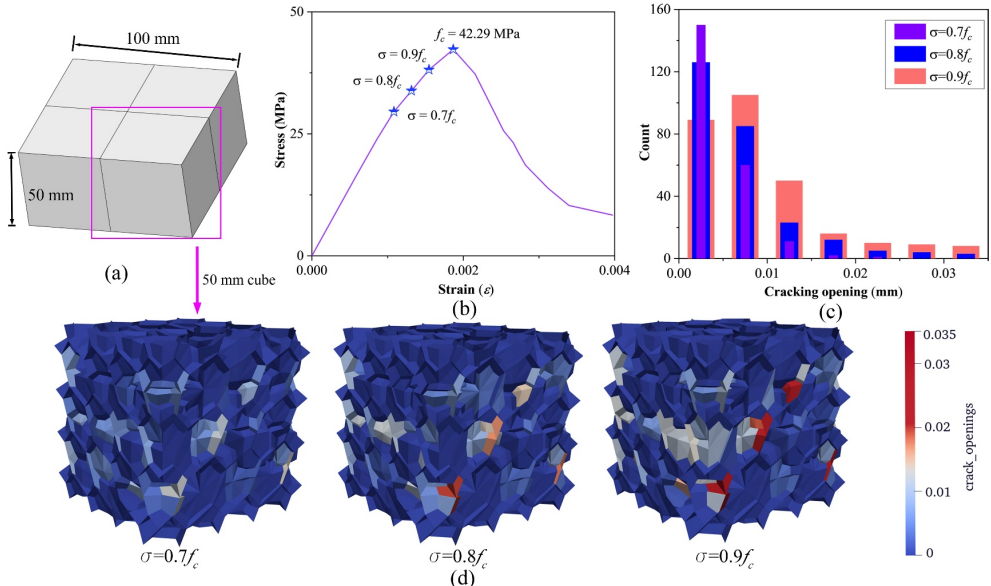


**FIGURE 5**  
Uniaxial compressive response of concrete members: (a) experimental specimen dimension; (b) stress-strain curve; (c) distribution of crack widths under different stress levels; (d) crack patterns.

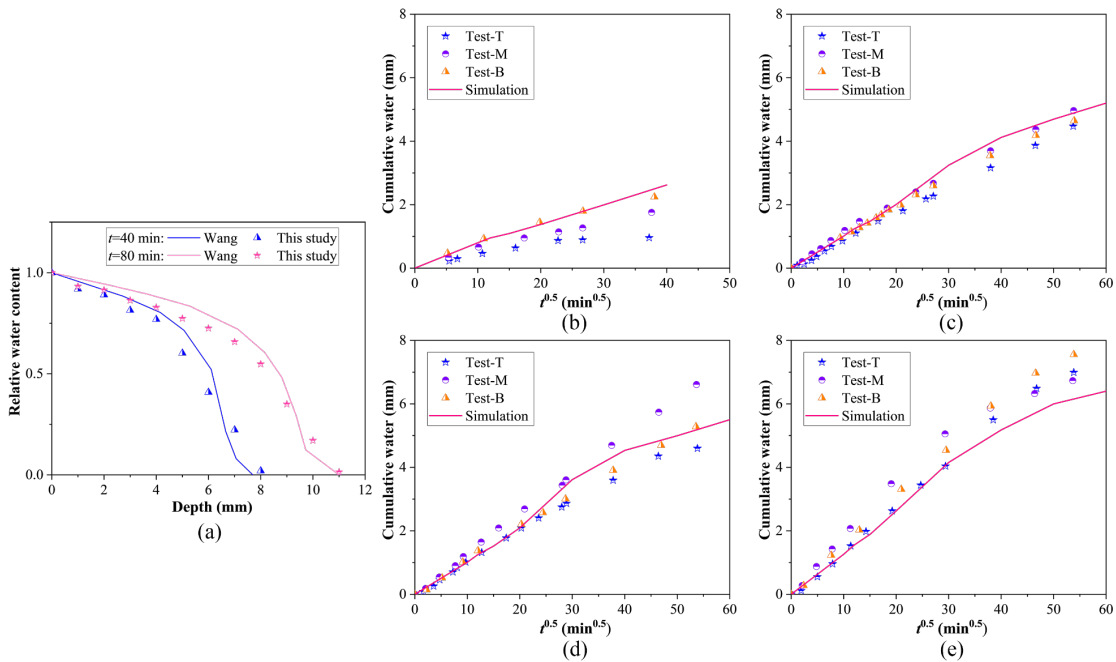


**FIGURE 6**  
Comparison between experimental and simulated results: (a)  $\theta$  – depth curves for unstressed conditions; (b)  $i - \sqrt{t}$  curves for unstressed conditions; (c)  $i - \sqrt{t}$  curves for  $\sigma = 0.7f_c$ ; (d)  $i - \sqrt{t}$  curves for  $\sigma = 0.8f_c$ ; (e)  $i - \sqrt{t}$  curves for  $\sigma = 0.9f_c$ .

## 4 | NUMERICAL RESULTS FOR WATER TRANSPORT

Given that chloride transport properties in unsaturated concrete are highly dependent on the water content, the first step in the validation of the model focuses on the coupled mechanical-water transport component of the proposed approach.

### 4.1 | Water transport of concrete under compression

Wang and Li (L. Wang & Li, 2014) performed a series of tests to explore the effect of microcracks on water absorption in concrete under tensile and compressive loading conditions with varying stress levels. The uniaxial compressive ( $f_c$ ) and tensile ( $f_t$ ) strengths of the concrete specimens of size  $100 \times 100 \times 200 \text{ mm}$  were reported as  $41.2 \pm 3.2 \text{ MPa}$  and  $3.6 \pm 0.3 \text{ MPa}$ , respectively. In the first set of tests, uniaxial compression with stress levels of  $0.7\sim0.9f_c$  was applied to concrete specimens to induce microcracks. Then, three sub-specimens of size  $100 \times 100 \times 50 \text{ mm}$  were obtained from the previously tested specimen and subjected to immersion testing. The three sub-specimens were labeled based on their original positions in the prismatic specimens, as follows: T (top), M (middle), and B (bottom). To speed up the computations, one quarter of the specimen is simulated with the proposed approach (see Figure 5(a)). In the mechanical LDPM, the bottom nodes were fully fixed, while vertical displacement was applied to the top nodes to simulate uniaxial loading. The concrete material properties employed in the mechanical LDPM simulations are summarized in Table 1.

Figure 5(b) shows that the mechanical model captures a compressive strength of  $42.29 \text{ MPa}$ , closely aligning with the experimental average value. Figures 5(c)-(d) report the simulated crack patterns and the distributions of crack widths in the concrete at different stress levels, which exhibits the expected significant increase in crack number and width with increasing stress level.

The transport lattice network model was then generated based on the mesh configuration of the mechanical LDPM, with crack widths calculated in the mechanical model mapped to the transport lattice elements using the proposed method. For water transport analysis, the relative water content for the bottom nodes in the transport lattice network model was set to 1, while all other nodes were initialized with a user-defined small quantity (0.01 in the reported simulations) to initiate the computation. The initial water diffusivity was set as  $D_{w,0} = 0.025 \text{ mm}/\text{min}$  for undamaged concrete (L. Wang & Li, 2014), while the value for the damaged lattice elements was calculated by means of

Equation (9).

Figure 6(a) shows the value of the relative water content distribution ( $\theta$ ) with respect to depth at  $t = 40 \text{ min}$  and  $t = 80 \text{ min}$  estimated by the coupled LDPM approach, which fundamentally agree with the theoretical calculations reported in the research (L. Wang & Li, 2014) using the one-dimensional unsaturated flow theory. Moreover, as shown in Figures 6(b)-(e), the simulated cumulative water content  $i$  with respect to time for concrete cubes under unstressed conditions and  $0.7\sim0.9f_c$  stress levels align well with the experimental measurements, both in the initial stage and the secondary stage, thereby validating the effectiveness of the proposed two-stage relationship between water diffusivity and crack width. Additionally, Figure 7 reports  $\theta$  in the elements under varying stress levels after 100, 500, and 1000 min of exposure. Results demonstrate that, when compared to the unstressed conditions, the water penetration depth in stressed concrete is significantly increased, particularly for the highest stress level for which the cracking is most pronounced.

### 4.2 | Water transport of concrete under tension

In a subsequent set of tests from Wang and Li, three tensile stress levels of  $0.7\sim0.9f_t$  were applied on the prismatic specimens to induce tensile microcracks (L. Wang & Li, 2014), with all other conditions matching the compression tests previously presented. After mechanical testing, two sub-specimens, denoted as Test-1 and Test-2, were cut from the specimens and used for immersion testing. The same LDPM discretization employed for the compression case was used to simulate the tensile testing. Figure 8(a) shows that the simulated tensile strength is approximately  $3.75 \text{ MPa}$ , which matches well with the experimental value of  $3.6 \pm 0.3 \text{ MPa}$ . Figure 8(b) reports the crack width distribution in the concrete due to the various tensile stress levels. As expected, cracks grow in both number and width as the level of the applied stress increases.

Figures 9(a)-(c) show that the predicted  $i - \sqrt{t}$  curves for the varying tensile stress levels are in excellent agreement with the experimental measurements, further validating the applicability of the proposed model. Moreover, the results demonstrate that the cumulative water content in damaged concrete is generally lower than that due to compressive loading, owing to differences in the crack distribution induced by compressive and tensile actions (see Figure 5(c) and Figure 8(b)). In addition, Figures 9(d)-(e) report the  $\theta - \text{depth}$  curves under various stress levels. Similarly to the compressive tests, the water depth penetration observed in the stressed cases is significantly higher than that of the control specimen.

TABLE 1 Material properties set for mechanical LDPM.

Experiment	Model size (mm)	Young's Modulus (MPa)	$f_c$ (MPa)	$f_t$ (MPa)	$f_s$ (MPa)	$G_t$ (N/mm)	$G_s$ (N/mm)
------------	-----------------	-----------------------	-------------	-------------	-------------	--------------	--------------

Wang & Li (2014)	50×50×50	45000	80	3.8	9.5	0.066	0.333
Zhang et al. (2014)	50×50×50	45000	60	3.2	8.0	0.056	0.28
Wang et al. (2019)	300×100×100	45000	100	4.0	10.0	0.07	0.35

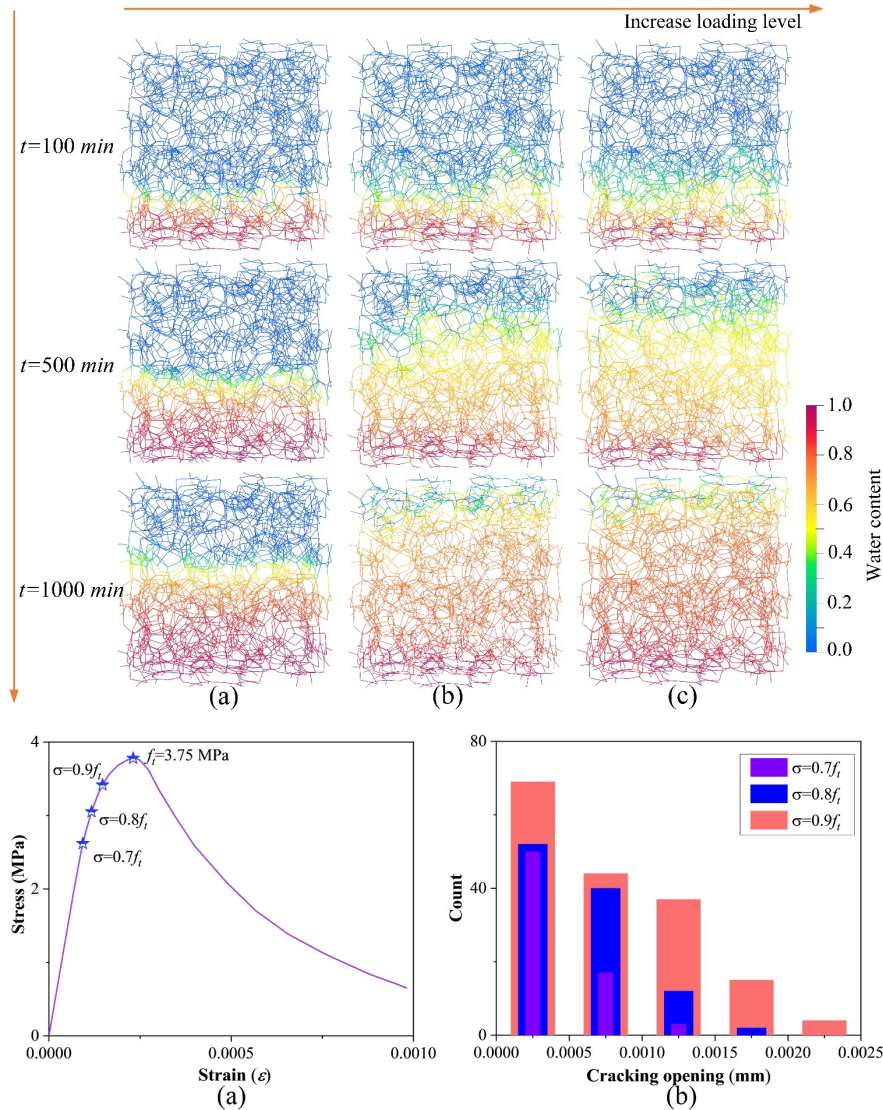


**FIGURE 7**  
Water transport in the elements, as predicted by the proposed coupled LDPM: (a) unstressed conditions; (b)  $\sigma = 0.7f_c$ ; (c)  $\sigma = 0.9f_c$ .

## 5 | NUMERICAL RESULTS CHLORIDE TRANSPORT ANALYSIS

### 5.1 | Chloride transport in concrete under short-term loading

Literature (L. Zhang et al., 2014) reports a series of immersion tests in a solution of water and NaCl, conducted on concrete specimens with cracking induced by uniaxial compression at stress levels of  $0.4 - 0.8f_c$ . The reported compressive strength was 34 MPa, with a Young's modulus of 27 GPa. Similarly to the previously reported simulations, a smaller domain with a size of 50 mm was simulated to speed up computations (as diagrammed in Figure 5(a)). All the material properties employed in the simulations are again summarized in Table 1. The calibrated material properties for LDPM capture the mechanical behavior of the test specimens

with satisfactory accuracy (see Figure 10(a)), with simulated values closely matching the experimental results. In addition, Figure 10(b) compares the crack width distributions for the stress conditions of  $0.4f_c$  (Point A),  $0.6f_c$  (Point B), and  $0.8f_c$  (Point C), exhibiting the expected behavior of growing crack widths with increased loading.

The transport lattice network was created based on the mechanical LDPM, and the crack widths were mapped to the transport elements. In accordance with the experimental conditions, where the lateral face (perpendicular to the loading direction) of the concrete cube was exposed to the NaCl solution, the chloride concentration applied to all nodes on this face in the transport LDPM is set to 0.65%, as reported from the experiments. The chloride diffusivity for the undamaged concrete (i.e., uncracked transport lattice elements) was set to  $1.0 \times 10^{-11} \text{ m}^2/\text{s}$ , consistent with the experimentally reported values.

**FIGURE 8**  
Numerical uniaxial tensile response of concrete elements: (a) stress-strain response; (b) distribution of crack widths at different stress levels.

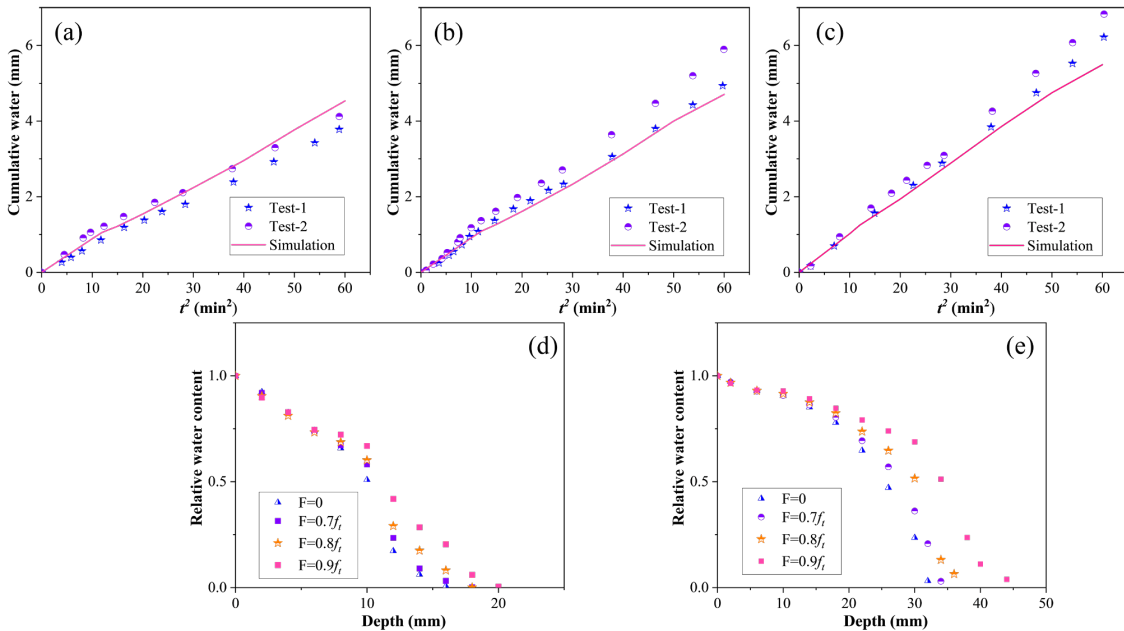


**FIGURE 9**  
Water transport analysis in concrete under tension: (a)  $i - \sqrt{t}$  curve for  $\sigma = 0.7f_t$ ; (b)  $i - \sqrt{t}$  curve for  $\sigma = 0.8f_t$ ; (c)  $i - \sqrt{t}$  curve for  $\sigma = 0.9f_t$ ; (d) simulated  $\theta$  – depth curves after 100 min exposure; (e) simulated  $\theta$  – depth curves after 1000 min exposure.

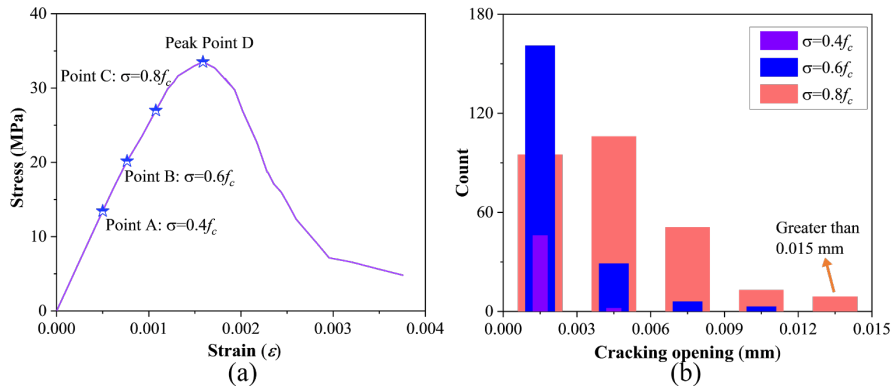


**FIGURE 10**  
Numeric al uniaxial compressive response: (a) stress-strain curve; (b) distribution of crack widths at different stress levels.

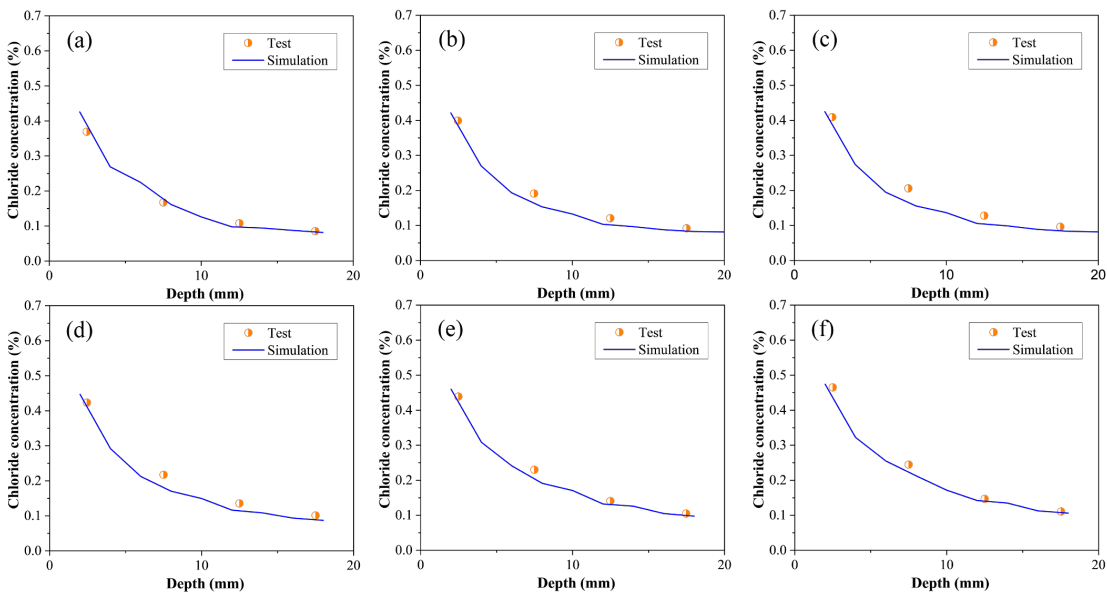


**FIGURE 11**  
Comparison between the experimental and simulated free chloride concentration-depth curves: (a) unstressed conditions; (b)  $\sigma = 0.4f_c$ ; (c)  $\sigma = 0.5f_c$ ; (d)  $\sigma = 0.6f_c$ ; (e)  $\sigma = 0.7f_c$ ; (f)  $\sigma = 0.8f_c$ .

Figure 11 compares the experimental and numerical free chloride concentration-depth curves after 56 days of exposure to the NaCl solution, indicating that the simulation both for the unstressed and stressed conditions closely agrees

with the experimental observations. Moreover, Figure 11 demonstrates that the free chloride concentration ( $C_f$ ) in concrete under the lowest stress level of  $0.4f_c$  is similar to that in the unstressed case. This can be attributed to the very limited cracks observed at this level of compressive stress (see

Figure 10(b)). As the loading increases, cracking increases in both width and quantity, expanding the transport channels and forming more preferential channels, thereby accelerating CT. In addition, Figure 12 compares the influence of stress levels on the CT properties in concrete. As expected,  $C_f$  at the same depth becomes larger with an increase in stress level.

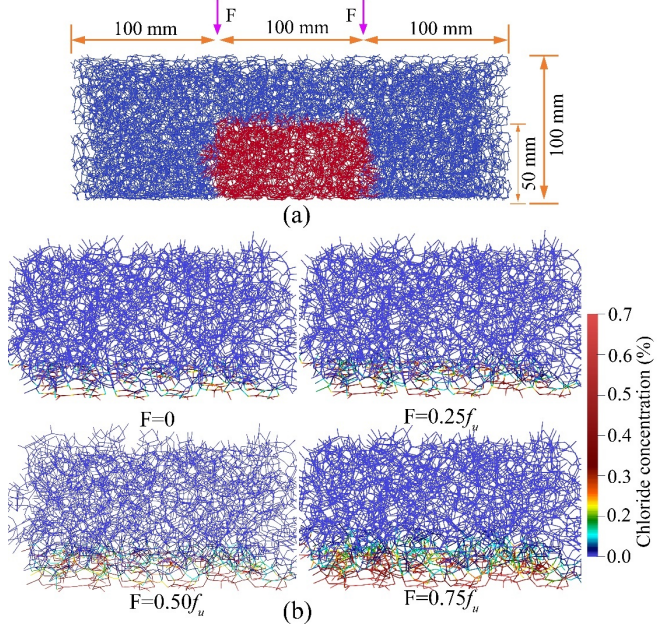
## 5.2 | Chloride transport in concrete under long-term loading

The literature (J. Wang et al., 2019) performed a series of chloride immersion tests on concrete elements after long-term 4-point bending loading. The specimens had a cross-section of  $100 \times 100 \text{ mm}$  and a clear span of  $300 \text{ mm}$ . In constructing the mechanical lattice network model, 1137 particles with sizes of  $5 \sim 10 \text{ mm}$  (as determined by the reported sieve curve) were randomly placed in the domain, leading to the generation of 11252 mechanical lattice elements (see Figures 13 and 14). The material properties used in the simulations are reported in Table 1. Consistently with the experimental setup, external forces were applied on the top of the concrete beam, to obtain a  $100 \text{ mm}$  pure bending portion in the middle of the specimen (see Figure 14(a)). A monotonic displacement loading was first applied to determine the ultimate capacity ( $f_u$ ), which is represented by the solid curves in Figure 13(a). Subsequently, loadings equivalent to  $0.25f_u$ ,  $0.50f_u$ , and  $0.75f_u$  were applied to simulate the long-term loading experimental protocol (dashed lines in Figure 13(a)).

Figures 13(b)-(c) report the distribution of cracks in the beam subjected to 60 days of sustained loading. As expected, higher loading levels result in greater cracking potential, with several macroscopic cracks observed at the bottom of the specimen under the highest loading condition considered. In addition, Figure 13(b) shows the crack development of a mechanical lattice element resulting from the long-term loading effect, indicating that cracks significantly propagate as a result of viscous effects.

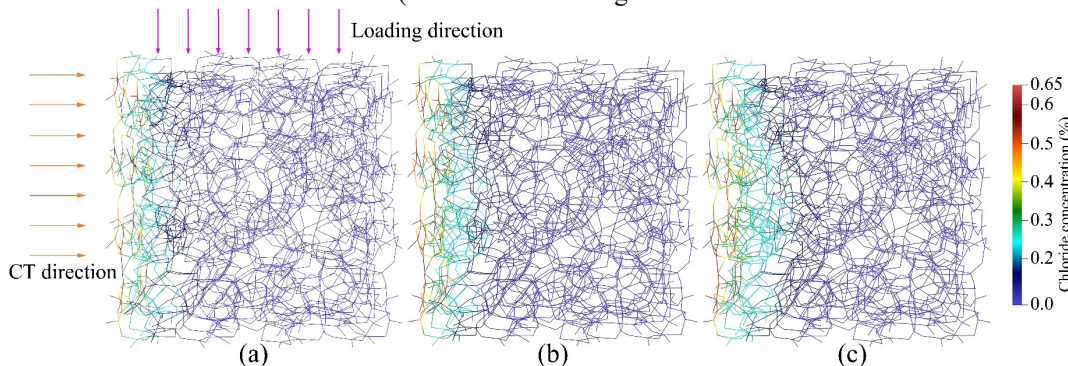
In the reported experiments, the bottom of the constant moment portion of the beam, the area of interest (AOI), was used for the immersion tests. In this context, to improve computing efficiency, only the nodes and transport lattice elements in the middle-bottom part of concrete beams were extracted from the overall model (red elements in Figure

14(a)) to be analyzed. Based on the experimental results, the chloride content applied to the concrete surface for the LDPM CT simulation was set to 0.7%. The chloride diffusion coefficient for the unstressed concrete specimen was set to  $0.934 \times 10^{-11} \text{ m}^2/\text{s}$ , as reported in the experiments. For the water transport analysis, the relative water content for the bottom nodes of the transport lattice network model was set to 1 to simulate immersion.



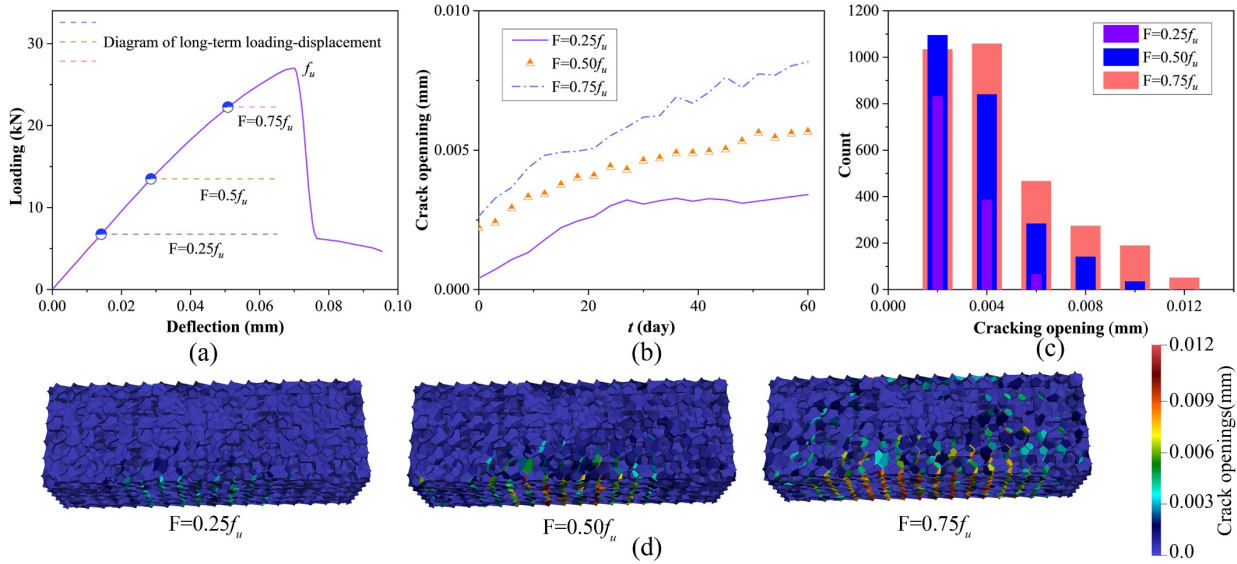
**FIGURE 14** Transport LDPM under long-term loadings: (a) AOI (red struts) for chloride transport analysis; (b) the free chloride concentration in the AOI after 60 days of loading.

Figure 15 reports comparison of the simulated and experimental measurements of  $C_f$  in the specimens after 30 and 60 days of exposure. Results demonstrate that the estimated  $C_f$  curves achieve good agreement with the experimental results. Furthermore, Figure 14(b) reports the distribution of chloride concentration after 60 days of loading and exposure. The first observation is that the penetration depth for the unstressed concrete is relatively small (approximately 4 mm), whereas, for higher loading levels, the predicted value is significantly larger (approximately 8 mm). In addition, the ion concentration for unstressed concrete is significantly lower than that of the loaded conditions.



**FIGURE 12** The effect of microcracks on chloride transport in concrete after 56 days of exposure: (a) unstressed conditions; (b)  $\sigma =$

$0.6f_c$ ; (c)  $\sigma = 0.8f_c$ .



**FIGURE 13** Concrete beams under long-term loadings with varying levels: (a) loading-deflection curves; (b) cracking propagation of a lattice element caused by the long-term loading effect; (c) distribution of crack width in concrete after 60 days of loadings; (d) cracking patterns in concrete beams after 60 days of loadings.

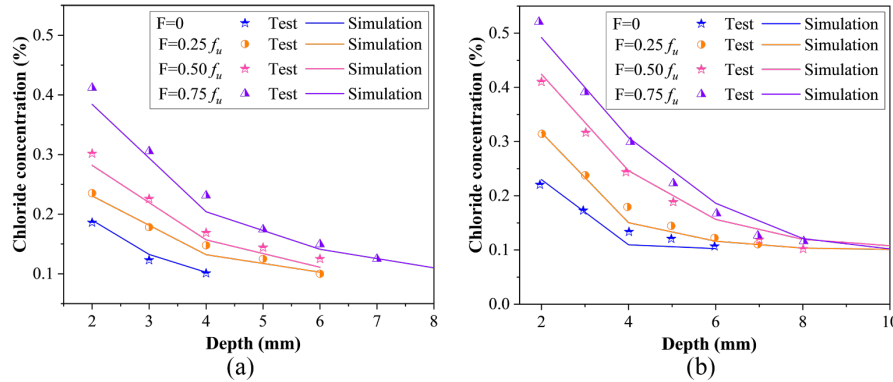


**FIGURE 15** Comparison between the experimental and numerical free chloride concentration distributions after (a) 30 and (b) 60 days of loading and exposure.

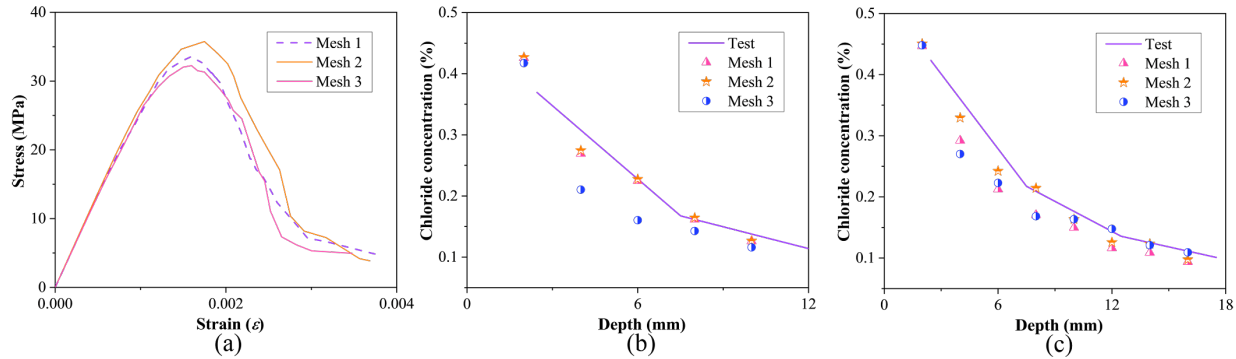


**FIGURE 16** Mesh sensitivity analysis: (a) stress-strain response of different meshes; (b) chloride concentration in the unstressed concrete simulated by different meshes; (c) chloride concentration in the concrete under a compressive stress level of  $0.8f_c$  simulated by different meshes.

## 6 | DISCUSSION

### 6.1 | Mesh sensitivity

A mesh sensitivity analysis was conducted to demonstrate the consistency of the modeling approach. Two additional LDPM

simulations with the same aggregate configuration were generated, referred to as Mesh 2 and Mesh 3, while the original lattice network used for the results presented in Section 5.1 is denoted as Mesh 1.

As expected, the simulated compressive stress-strain curves of the three models are in agreement (see Figure 16(a)).

Furthermore, Figures 16(b)-(c) compare the  $C_f$  – depth curves in the unstressed and stressed concrete with a loading level of  $0.8f_c$ . Results show that the numerical predictions are in agreement with the experimental results and with each other. The consistency among the three models with different meshes indicates that the proposed model is stable with respect to the randomly generated lattice network and reliable for investigating the effect of microcracks induced by varying levels of loading on the global chloride transport properties in concrete.

## 6.2 | Effect of relative water content

In this section, the coupled LDPM approach is exercised to study the effect of the relative water content in the specimens. In particular, the following five cases were selected:  $\theta = 0$  (dry conditions),  $\theta = 0.25$ ,  $\theta = 0.50$ ,  $\theta = 0.75$ , and  $\theta = 1$  (fully saturated conditions). As reported in Figure 17, in dry environments, penetration is minimal, with a penetration depth of around 3 mm and an ion concentration of approximately 0.2% at 2 mm depth. In contrast, higher water content significantly accelerates chloride ingress, particularly in saturated conditions. For instance, penetration depth increases significantly, reaching up to 14 mm in the saturated conditions. These observations underscore the critical role of water, especially higher water contents, in accelerating chloride penetration.

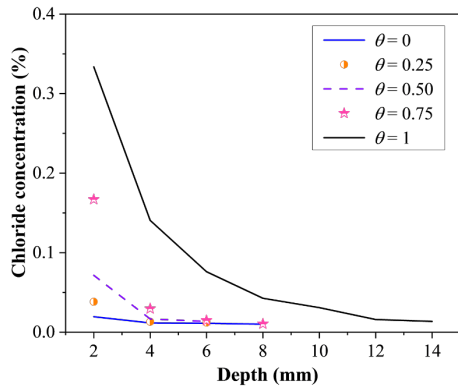


FIGURE 17 Effect of the relative water content on chloride transport properties.

## 6.3 | Effect of long-term loading

The model used in the 4-point bending tests described in Section 5.2 was also employed to study the effect of short- and long-term loadings on CT. Figure 18 reports the  $C_f$  – depth curves under short- and long-term ( $t = 60$  days) loading conditions. Results demonstrate that in the long-term loading conditions the free chloride concentration is approximately 2 times larger than that predicted for the short-term loading case. Moreover, the ion penetration depth is also predicted to be significantly greater for the long-term loading conditions. This significant acceleration of ion intrusion can be attributed to the formation of denser crack networks in the

specimens under long-term loading. As illustrated in Figure 13(b), cracks in the concrete for 60 days of loading increase significantly regardless of the loading magnitude, thereby widening the conduit for the transport. Therefore, the effect of long-term loading on the chloride transport analysis is expected to be significant when analyzing the transport properties of cementitious composites.

## 7 | CONCLUSIONS

In this study, a coupled LDPM approach was proposed to describe transport properties in cracked concrete elements subjected to short- and long-term loading conditions. A mechanical lattice is first employed to predict crack networks induced by various types of loadings, including creep behavior under long-term loading conditions, as described by viscous strain effects in the model formulation. Such information is then mapped on a dual transport lattice network, enabling one way coupling of the micro- and macrocracks onto the transport properties of the lattice elements. A new formulation for the relationship between the diffusivity coefficient and the crack width is proposed, which enables accurate assessment of the effects of microscopic cracking on the transport properties of the material. In addition to the diffusion mechanism, the model is capable of describing convection arising from capillary absorption. The proposed model was validated by means of independent water absorption and CT experiments on concrete members subjected to compression, tension, and 4-point bending actions. The main conclusions can be summarized below:

- (1) The prediction of water absorption and chloride transport in cracked concrete members under different types of loading with varying stress levels agrees with the experimental results well, indicating that the proposed coupled LDPM is capable of capturing the effect of micro- and macro-cracks on the transport properties of the elements.
- (2) The comparison of experimental and numerical results on chloride concentrations in cracked concrete under long-term loading conditions validates the capability of the proposed model to predict the cracking propagation and mass transport properties in concrete in the presence of viscous effects.
- (3) The relative water content has a significant influence on CT properties, as it accelerates the chloride diffusion, while long-term loadings can significantly accelerate the chloride intrusion by inducing more mechanical damage.
- (4) The proposed coupled LDPM demonstrates robustness and stability in predicting CT properties in both unstressed and stressed concrete members.

One limitation of the proposed coupled LDPM is that it does not account for the impact of viscoelastic-induced cracking on the transport properties of concrete components under long-term loading, requiring further research to quantify this effect.

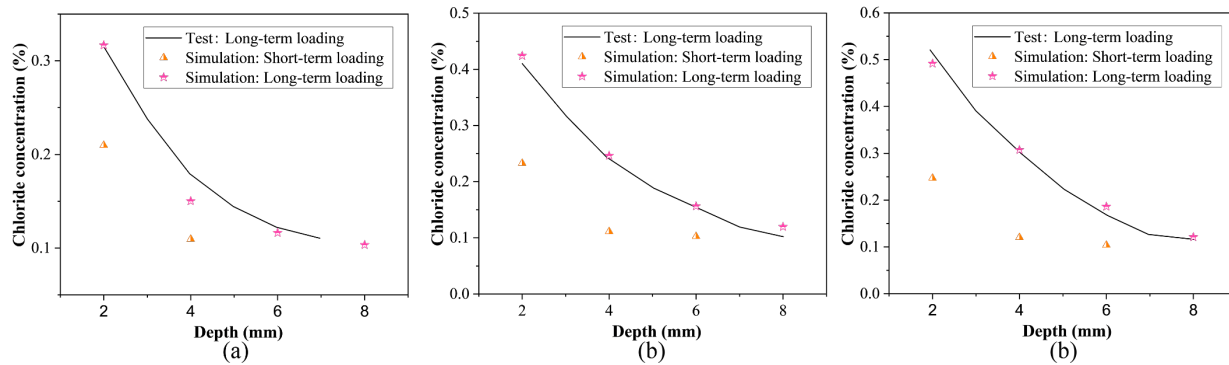


**FIGURE 18** Comparison of the chloride concentration in the concrete under short-term and long-term loadings: (a)  $F = 0.25f_u$ ; (b)  $F = 0.50f_u$ ; (c)  $F = 0.75f_u$ .

## 8 | REFERENCES

- Abdellatef, M., Boumakis, I., Wan-Wendner, R., & Alnaggar, M. (2019). Lattice Discrete Particle Modeling of concrete coupled creep and shrinkage behavior: A comprehensive calibration and validation study. *Construction and Building Materials*, 211, 629–645.
- Abyaneh, S. D., Wong, H. S., & Buenfeld, N. R. (2016). Simulating the effect of microcracks on the diffusivity and permeability of concrete using a three-dimensional model. *Computational Materials Science*, 119, 130–143.
- Bentz, D. P., Garboczi, E. J., Lu, Y., Martys, N., Sakulich, A. R., & Weiss, W. J. (2013). Modeling of the influence of transverse cracking on chloride penetration into concrete. *Cement and Concrete Composites*, 38, 65–74.
- Bousikhane, F., Li, W., Di Luzio, G., & Cusatis, G. (2018). Full coupling between diffusion and mechanical analysis in a discrete computational framework. In *Computational Modelling of Concrete Structures* (pp. 305–310). CRC Press.
- Cibelli, A., Luzio, G. Di, & Ferrara, L. (2023). Numerical Simulation of the Chloride Penetration in Cracked and Healed UHPC via a Discrete Multiphysics Model. *Journal of Engineering Mechanics*, 149(12), 5023001.
- Cusatis, G., Pelessone, D., & Mencarelli, A. (2011). Lattice Discrete Particle Model (LDPM) for failure behavior of concrete. I: Theory. *Cement and Concrete Composites*, 33(9), 881–890.
- de Vera, G., Climent, M. A., Viqueira, E., Antón, C., & Andrade, C. (2007). A test method for measuring chloride diffusion coefficients through partially saturated concrete. Part II: The instantaneous plane source diffusion case with chloride binding consideration. *Cement and Concrete Research*, 37(5), 714–724.
- Di Luzio, G., & Cusatis, G. (2013). Solidification-microprestress-microplane (SMM) theory for concrete at early age: Theory, validation and application. *International Journal of Solids and Structures*, 50(6), 957–975.
- Djerbi Tegguer, A., Bonnet, S., Khelidj, A., & Baroghel-Bouny, V. (2013). Effect of uniaxial compressive loading on gas permeability and chloride diffusion coefficient of concrete and their relationship. *Cement and Concrete Research*, 52, 131–139.
- Eliáš, J., & Cusatis, G. (2022). Homogenization of discrete mesoscale model of concrete for coupled mass transport and mechanics by asymptotic expansion. *Journal of the Mechanics and Physics of Solids*, 167, 105010.
- Fascetti, A., Bolander, J. E., & Nisticó, N. (2018). Lattice Discrete Particle Modeling of Concrete under Compressive Loading: Multiscale Experimental Approach for Parameter Determination. *Journal of Engineering Mechanics*, 144(8), 4018058.
- Fascetti, A., Ichimaru, S., & Bolander, J. E. (2022). Stochastic lattice discrete particle modeling of fracture in pervious concrete. *Computer-Aided Civil and Infrastructure Engineering*, 37(14), 1788–1808.
- Fascetti, A., & Oskay, C. (2019a). Dual random lattice modeling of backward erosion piping. *Computers and Geotechnics*, 105, 265–276.
- Fascetti, A., & Oskay, C. (2019b). Multiscale modeling of backward erosion piping in flood protection system infrastructure. *Computer-Aided Civil and Infrastructure Engineering*, 34(12), 1071–1086.
- Federal Highway Administration. (2002). *Corrosion Cost and Preventive Strategies in the United States*.
- Grassl, P. (2009). A lattice approach to model flow in cracked concrete. *Cement and Concrete Composites*, 31(7), 454–460.
- Grassl, P., & Bolander, J. (2016). Three-Dimensional Network Model for Coupling of Fracture and Mass Transport in Quasi-Brittle Geomaterials. *Materials*, 9(9).
- Hall, C. (1989). Water sorptivity of mortars and concretes: a review. *Magazine of Concrete Research*, 41(147), 51–61.
- Ismail, M., Toumi, A., François, R., & Gagné, R. (2004). Effect of crack opening on the local diffusion of chloride in inert materials. *Cement and Concrete Research*, 34(4), 711–716.
- Jia, D., Brigham, J. C., & Fascetti, A. (2024). An efficient static solver for the lattice discrete particle model. *Computer-Aided Civil and Infrastructure Engineering*.
- Li, W., & Guo, L. (2020). A mechanical-diffusive peridynamics coupling model for meso-scale simulation of chloride penetration in concrete under loadings. *Construction and Building Materials*, 241.
- Li, W., Zhou, X., Carey, J. W., Frash, L. P., & Cusatis, G. (2018). Multiphysics Lattice Discrete Particle Modeling (M-LDPM) for the Simulation of Shale Fracture Permeability. *Rock Mechanics and Rock Engineering*, 51(12), 3963–3981.
- Li, Y., Chen, X., Jin, L., & Zhang, R. (2016). Experimental and numerical study on chloride transmission in cracked

- concrete. *Construction and Building Materials*, 127, 425–435.
- Lim, C. C., Gowripalan, N., & Sirivivatnanon, V. (2000). Microcracking and chloride permeability of concrete under uniaxial compression. *Cement and Concrete Composites*, 22(5), 353–360.
- Liu, J., Ou, G., Qiu, Q., Chen, X., Hong, J., & Xing, F. (2017). Chloride transport and microstructure of concrete with/without fly ash under atmospheric chloride condition. *Construction and Building Materials*, 146, 493–501.
- Liu, Q., Hu, Z., Wang, X., Zhao, H., Qian, K., Li, L. jie, & Meng, Z. (2022). Numerical study on cracking and its effect on chloride transport in concrete subjected to external load. *Construction and Building Materials*, 325.
- Lockington, D. (1993). Estimating the Sorptivity for a Wide Range of Diffusivity Dependence on Water Content. In *Transport in Porous Media* (Vol. 10). Kluwer Academic Publishers.
- Lockington, D., Parlange, J.-Y., & Dux, P. (1999). Sorptivity and the estimation of water penetration into unsaturated concrete. *Materials and Structures*, 32, 342–347.
- Peng, J., Hu, S., Zhang, J., Cai, C. S., & Li, L. yuan. (2019). Influence of cracks on chloride diffusivity in concrete: A five-phase mesoscale model approach. *Construction and Building Materials*, 197, 587–596.
- Qiu, Q., & Dai, J.-G. (2021). Meso-scale modeling of chloride diffusivity in mortar subjected to corrosion-induced cracking. *Computer-Aided Civil and Infrastructure Engineering*, 36(5), 602–619.
- Saeki, T., & Niki, H. (1996). *Migration of chloride ions in non-saturated mortar*. 963–968.
- Šavija, B., Luković, M., & Schlangen, E. (2014). Lattice modeling of rapid chloride migration in concrete. *Cement and Concrete Research*, 61–62, 49–63.
- Šavija, B., Pacheco, J., & Schlangen, E. (2013). Lattice modeling of chloride diffusion in sound and cracked concrete. *Cement and Concrete Composites*, 42, 30–40.
- Sciumè, G., & Benboudjema, F. (2017). A viscoelastic Unitary Crack-Opening strain tensor for crack width assessment in fractured concrete structures. *Mechanics of Time-Dependent Materials*, 21(2), 223–243.
- Tong, L., Liu, Q., Xiong, Q., Meng, Z., Amiri, O., & Zhang, M. (2024). Modeling the chloride transport in concrete from microstructure generation to chloride diffusivity prediction. *Computer-Aided Civil and Infrastructure Engineering*.
- Tran, T. T., Pham, D. T., Vu, M. N., Truong, V. Q., Ho, X. B., Tran, N. L., Nguyen-Sy, T., & To, Q. D. (2021). Relation between water permeability and chloride diffusivity of concrete under compressive stress: Experimental investigation and mesoscale lattice modelling. *Construction and Building Materials*, 267.
- Wang, J., Niu, D., Wang, Y., He, H., & Liang, X. (2019). Chloride diffusion of shotcrete lining structure subjected to nitric acid, salt–frost degradation, and bending stress in marine environment. *Cement and Concrete Composites*, 104.
- Wang, L., Bao, J., & Ueda, T. (2016). Prediction of mass transport in cracked-unsaturated concrete by mesoscale lattice model. *Ocean Engineering*, 127, 144–157.
- Wang, L., & Li, S. (2014). Capillary absorption of concrete after mechanical loading. *Magazine of Concrete Research*, 66(8), 420–431.
- Wang, L., & Ueda, T. (2014). Mesoscale Modeling of Chloride Penetration in Unsaturated Concrete Damaged by Freeze-Thaw Cycling. *Journal of Materials in Civil Engineering*, 26(5), 955–965.
- Wang, Z., Oskay, C., & Fascetti, A. (2024). Three-dimensional numerical modeling of the temporal evolution of backward erosion piping. *Computers and Geotechnics*, 171, 106381.
- Xi, Y., & Bažant, Z. P. (1999). Modeling Chloride Penetration in Saturated Concrete. *Journal of Materials in Civil Engineering*, 11(1), 58–65.
- Yang, Z., Weiss, W. J., & Olek, J. (2006). Water Transport in Concrete Damaged by Tensile Loading and Freeze-Thaw Cycling. *Journal of Materials in Civil Engineering*, 18(3), 424–434.
- Zhang, L., Jia, J., Meng, G., & Zhu, W. (2014). Chloride diffusion in concrete subjected to compressive loading. *Magazine of Concrete Research*, 66(19), 991–997.
- Zhang, Y., Zhang, M., & Ye, G. (2018). Influence of moisture condition on chloride diffusion in partially saturated ordinary Portland cement mortar. *Materials and Structures/Materiaux et Constructions*, 51(2).
- Zhang, Y., Zhang, S., Wei, G., Wei, X., Jin, L., & Xu, K. (2019). Water transport in unsaturated cracked concrete under pressure. *Advances in Civil Engineering*, 2019.
- Zheng, B., Li, T., Qi, H., Gao, L., Liu, X., & Yuan, L. (2022). 3D meso-scale simulation of chloride ion transportation in cracked concrete considering aggregate morphology. *Construction and Building Materials*, 326.
- Zhu, Y., & Fascetti, A. (2024). Towards Developing Reinforced Concrete Structures Digital Twins: A Multiscale Lattice Discrete Particle Model Approach. *Advances in Structural Engineering*.